

Vortex-Ring-Induced Stratified Mixing: Mixing Model

Jason Olsthoorn[†], and Stuart B. Dalziel

Department of Applied Mathematics and Theoretical Physics, University of Cambridge,
Centre for Mathematical Sciences, Wilberforce Road, Cambridge UK, CB3 0WA

(Received ?; revised ?; accepted ?. - To be entered by editorial office)

The study of vortex-ring-induced mixing has been significant for understanding stratified turbulent mixing in the absence of a mean flow. Renewed interest in this topic has prompted the development of a one-dimensional model for the evolution of a stratified system in the context of isolated mixing events. This model is compared to numerical simulations and physical experiments of vortex rings interacting with a stratification. Qualitative agreement between the evolution of the density profiles is observed, along with close quantitative agreement of the mixing efficiency. This model highlights the key dynamical features of such isolated mixing events.

1. Introduction

Understanding the mixing produced by turbulent motion in a stratified environment remains elusive. Such mixing is particularly relevant in an oceanographic context (Ivey *et al.* 2008). The energy cascade found in turbulent flows results in a large range of length scales, which complicates the analysis. However, Turner (1968), while examining grid-generated stratified turbulence (with no mean flow), argued that most of the mixing of the density field was generated by independent localized mixing events, resulting from large-scale turbulent eddies impacting the density interface. These findings motivated Linden (1973) to study isolated vortex-ring mixing events as an analogy to the intermittent large-eddy dynamics. Vortex rings provide a reproducible coherent structure of vorticity with defined length and velocity scales, making them the ideal candidate for studying turbulent-eddy mixing events. Indeed, Linden's work on vortex rings has had a significant impact on the stratified turbulence literature (Linden 1979; Fernando 1991). Recent advances in experimental fluid mechanics have prompted a return to these vortex-ring experiments. Direct measurements of the density field evolution as a result of vortex-ring-induced mixing events have been recently presented in Olsthoorn & Dalziel (2015). The current paper presents a one-dimensional (1D) model for the mixing induced by isolated mixing events driven by a source of coherent (non-turbulent) energy, such as the mixing induced by a sequence of vortex rings. In this discussion, we will focus on mixing events with a length scale larger than the thickness of the density interface. Understanding the fluid mixing that occurs in this simplified context provides insight into the mixing produced by fully developed stratified turbulence.

Building on the work of Balmforth *et al.* (1998), we model the stratified vortex-ring experiments as a coupled system of equations for the coherent vortex ring energy density (T), stirring energy density (e) and the background (sorted) density field (ρ). To ensure the validity of this approach, we compare the model results with both numerical simulations of the mixing events (presented here) and the experimental results of Olsthoorn &

[†] Email address for correspondence: Jason.Olsthoorn@cantab.net

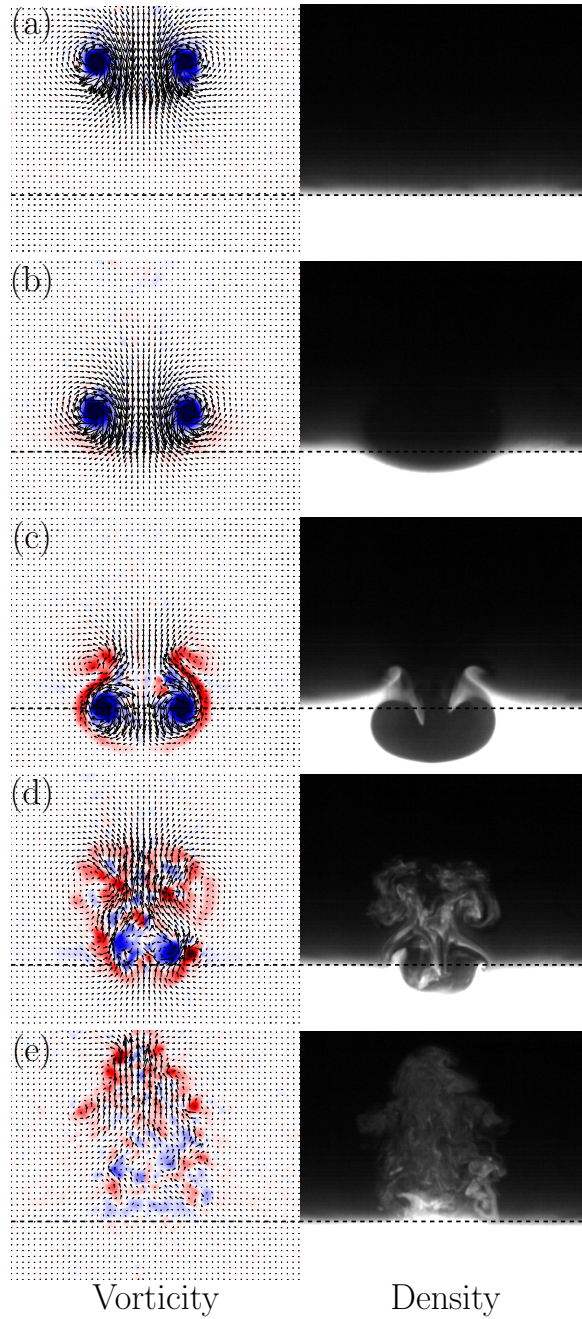


Figure 1: Representative snapshots of a stratified vortex-ring experiment provided every two advective time units. This plot presents the computed azimuthal vorticity field with overlaid velocity field vectors (left) and the evolution of the density field (right) within a vertical light sheet. A dashed line as been added to denote the estimated initial position of the density interface. The experimental details associated with this figure are provided in Olsthoorn & Dalziel (2017). For reference, the parameters associated with this experiment are $Re = 2400$, $Ri = 2.3$.

42 Dalziel (2015). The mixing efficiency, calculated for all three methodologies, is shown to
 43 be highly consistent.

44 The remainder of this discussion is organized as follows: §2 describes the mechanical
 45 and dynamical evolution of the physical vortex-ring experiments. Section 3 then details
 46 the construction of a 1D mixing model to predict the mixing within such a system. These
 47 model results are supplemented with numerical simulations, as described in §4. Finally,
 48 §5 compares the mixing efficiency results for all three methodologies, and summarizes
 49 these findings.

50 2. Description of the Physical Vortex-Ring-Induced Mixing 51 Experiments

52 We attempt to model the mixing produced by a large number of independent vortex-
 53 ring-induced mixing experiments. Physical measurements of such a system have been
 54 recently reported in Olsthoorn & Dalziel (2015). In each of those experiments, a tank was
 55 initially filled with a stable density stratification consisting of two nearly-homogeneous
 56 layers with a sharp density transition between them. For the remainder of this paper,
 57 we will denote this type of stratification as a ‘continuous two-layer stratification’, with
 58 the understanding that the stratification is approximately two-layer with a continuous
 59 transition region between them. A sequence of vortex rings were then generated within
 60 the tank, such that they propagated along the direction of gravity. The maximum distance
 61 below the interface that any vortex ring penetrated was small compared with the depth
 62 of the lower layer fluid, such that the bottom of the tank did not significantly affect the
 63 dynamics of the flow. As each vortex ring translated under its self-induced velocity, it
 64 displaced the isosurfaces of the density field. The perturbation to the density field resulted
 65 in the production of secondary vorticity through a baroclinic torque. This secondary
 66 vorticity was produced directly at the location of the density interface. Lawrie & Dalziel
 67 (2011) have previously argued that the co-location of vorticity with the peak density
 68 gradients, as was the case in these experiments, will lead to a high mixing efficiency.
 69 Further, in a recent publication, Olsthoorn & Dalziel (2017) have demonstrated that the
 70 coupling of the secondary vorticity with the impinging vortex ring results in an instability
 71 that rapidly generates turbulence. Thus, to review, each propagating vortex ring displaces
 72 the isopycnal surfaces, which produces secondary vorticity that, through an interaction
 73 with the vortex ring, is unstable to an instability identified in Olsthoorn & Dalziel (2017).
 74 The subsequent turbulent production further enhances the stirring of the density field,
 75 generating density fluctuations down to the Kolmogorov scale. In the experiments of
 76 Olsthoorn & Dalziel (2015), the time interval between the generation of each vortex ring
 77 was sufficient to allow the fluid within the tank to become nearly quiescent (except for
 78 thermal fluctuations). By measuring the density field between a sequence of these mixing
 79 events, Olsthoorn & Dalziel (2015) quantified the mixing induced by each vortex ring.

80 Figure 1 presents representative snapshots of a single stratified vortex-ring experiment.
 81 Although presented slightly differently, the experiment shown in figure 1 is the same as
 82 one of those presented in figure 2 of Olsthoorn & Dalziel (2017), to which the reader
 83 is referred for details on the experimental setup. Here, figure 1 shows the computed
 84 azimuthal vorticity field with overlaid velocity field vectors (left) and the evolution of
 85 the density field (right) within a vertical laser sheet. These equally spaced snapshots
 86 highlight the propagation of the vortex ring (figure 1(a)), the displacement of the density
 87 interface (figure 1(b)), followed by the production of secondary vorticity (figure 1(c)),
 88 the instability of the vortex ring (figure 1(d)), and the slow transition back to quiescence
 89 (figure 1(e)). While this figure has been generated from a single vortex-ring experiment,

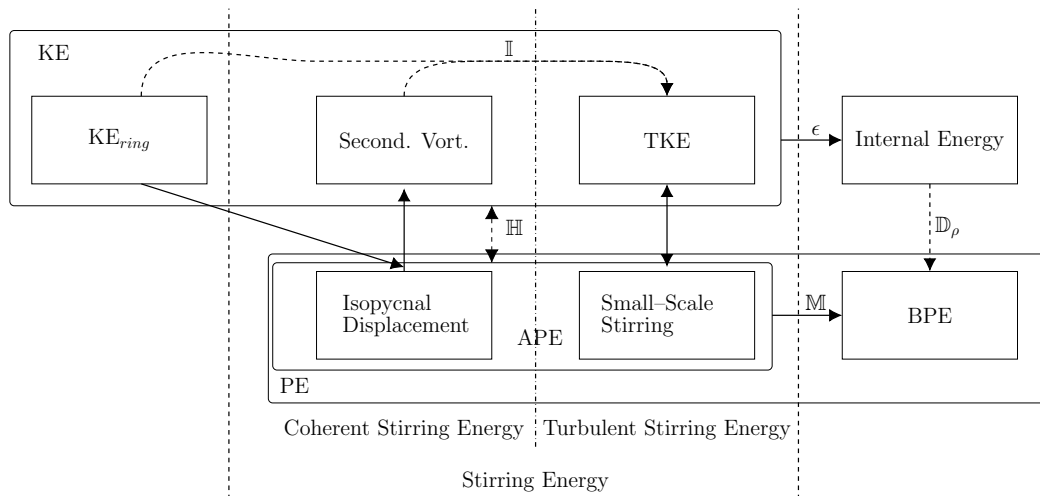


Figure 2: Diagram of the simplified energy pathway for the vortex ring experiments. The input of kinetic energy from the vortex ring (KE_{ring}) will lead to an increase in the gravitational potential energy (BPE) of the system. The size of each energy reservoir does not correspond to its relative contribution.

90 each of these five steps are characteristic of the vortex-ring experiments considered here.
 91 Note that the height of the mixing region is comparable to the diameter of the impacting
 92 vortex ring.

93 The above description of the vortex-ring experiment's mechanics highlights the stirring
 94 (and the associated production of strong density gradients) of the density field. This
 95 is only one component of mixing, which occurs through a combination of stirring and
 96 diffusion. In the vortex-ring experiments, the smallest scale features of the flow were
 97 produced through the turbulent eddies. Thus, we argue, that the majority of the fine
 98 scale stirring, and consequently the mixing, induced by the vortex ring will only occur
 99 once the flow becomes unstable to the instability discussed in Olsthoorn & Dalziel (2017).
 100 As we will see below, we construct our model such that the growth rate of the vortex-ring
 101 instability will limit the mixing rate.

Both a velocity and length scale are required in order to parameterize the vortex-ring-
 induced mixing. For the vortex-ring experiments, it is natural to select the vortex-ring
 propagation velocity U as the characteristic velocity, and the vortex-ring diameter a as
 the characteristic length scale. This paper focuses on three dimensionless parameters:
 the Reynolds number (Re , the ratio of inertia to viscous forces), the Richardson number
 (Ri , the ratio of buoyancy to advective forces), and the Schmidt number (Sc , the ratio
 of viscous to molecular diffusion). These are defined as

$$Re = \frac{Ua}{\nu}, \quad Ri = \frac{g(\rho_2 - \rho_1)}{\rho_1} \frac{a}{U^2}, \quad Sc = \frac{\nu}{\kappa}. \quad (2.1)$$

102 Here, g is the acceleration due to gravity, ρ_1, ρ_2 are densities associated with the strat-
 103 ification, ν is the kinematic viscosity (here, $\nu = 1 \times 10^{-6}$ m²/s) and κ is the coefficient
 104 of mass diffusion. In this paper, we will model the vortex-ring-induced mixing produced
 105 in the physical experiments and in numerical simulations (presented in §4). With each of
 106 these methodologies, we will ensure consistency by comparing the Reynolds, Richardson,
 107 and Schmidt numbers.

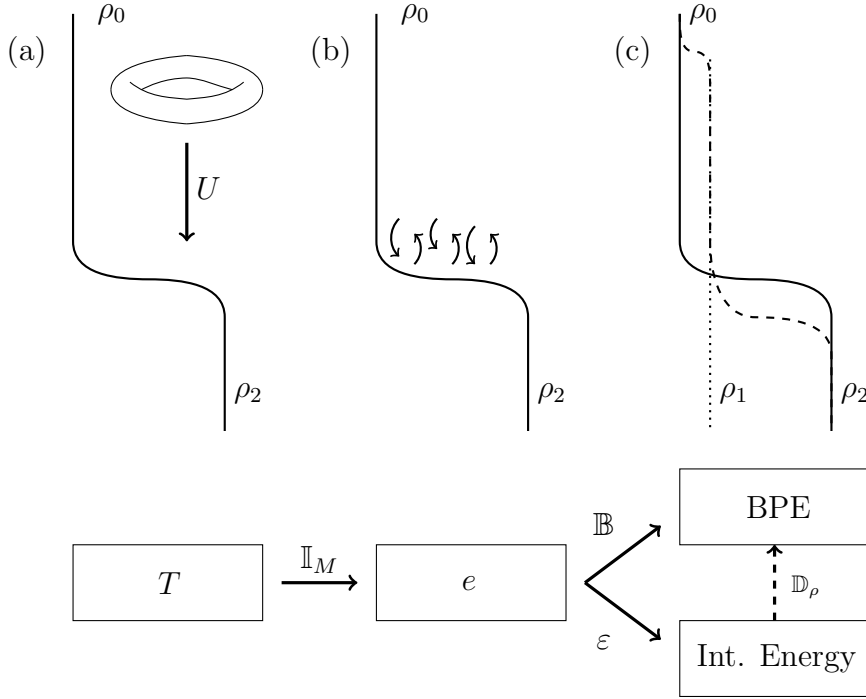


Figure 3: Diagram of the energy pathways in the model construction. The kinetic energy of the vortex ring $[T]$ (a) breaks down into stirring energy $[e]$ (b), which subsequently mixes the density profile $[\rho]$ (c) changing the background potential energy of the system [BPE].

Another important parameter is the kinetic energy of each vortex ring (KE_{ring}). According to Norbury (1973), the kinetic energy of a vortex ring is given as

$$\text{KE}_{ring} = C_{KE} \left(\frac{1}{2} \rho_1 U^2 \right) \left(\frac{4}{3} \pi \left(\frac{a}{2} \right)^3 \right). \quad (2.2)$$

108 The constant C_{KE} is a function of the vortex ring aspect ratio (the ratio of the core
109 width to ring diameter). For the vortex rings used in Olsthoorn & Dalziel (2015), a value
110 of $C_{KE} = 6.5$ has been estimated, and thus we use this value when discussing the model
111 experiments below.

112 Figure 2 presents a diagram of the energy pathways resulting from the input of KE_{ring} .
113 The propagating vortex ring produces available potential energy (APE, see Winters *et al.*
114 (1995)) by displacing the isopycnal surfaces from their equilibrium position that, in turn,
115 generates the kinetic energy (KE) associated with the secondary vorticity. In general,
116 KE will produce APE in the system (and vice versa) via a reversible buoyancy flux (\mathbb{H}).
117 The instability that results from the coupling of the primary vortex ring and secondary
118 vorticity then produces turbulent kinetic energy (TKE) at a rate \mathbb{I} . This TKE production
119 is coupled to (both generates and is generated by) the APE associated with the small
120 scale stirring of the density field that, through diffusion, mixes the stratification at some
121 rate \mathbb{M} , increasing the background potential energy (BPE) of the system. KE (predomi-
122 nantly through TKE) also viscously dissipates at a rate ϵ , acting as a source for internal
123 energy. Diffusion of the background density profile (\mathbb{D}_ρ) will also slowly increase the BPE

124 of the system. There are additional partitions of energy in the system, such as internal
 125 waves, that are not specifically labeled within figure 2 as these other energy reservoirs
 126 do not significantly contribute to the dominant mixing mechanism. This description of
 127 the energy pathways is consistent with the work of Winters *et al.* (1995), who considered
 128 mixing in an oceanographic context. The total KE and APE, excluding KE_{ring} , will be
 129 denoted as stirring energy. Here, stirring is a result of both the coherent (reproducible)
 130 motions and the turbulent fluctuations. We denote the energy associated with the coher-
 131 ent motions as ‘coherent stirring energy’, and likewise, we denote the energy associated
 132 with the turbulent fluctuations as ‘turbulent stirring energy’. We argue that the turbu-
 133 lent fluctuations (turbulent stirring energy) are the dominant contributor to the change
 134 in the BPE of the system. We will return to this when we discuss the model construction.

135 In the experiments, once the transient stirring energy in the system had sufficiently
 136 dissipated, another vortex ring was generated and the cycle repeated. This process contin-
 137 ued until the desired number of vortex rings was generated. We will model the repetitive
 138 generation of vortex rings below.

139 3. Model of the Vortex-Ring-Induced Mixing Experiments

140 The purpose of the present model is to predict the mixing produced by isolated vortex-
 141 ring-induced mixing events within a stratified fluid. To characterize this system, we model
 142 the coherent vortex-ring energy density (T), the stirring energy density (e) and the
 143 background density field (ρ). We consider horizontally averaged quantities such that
 144 each variable is only a function of a single spatial (vertical) dimension and time. This
 145 model builds upon the conceptualization introduced in figure 2. As the majority of the
 146 mixing and dissipation will result from turbulent motions, we model e as a turbulent
 147 quantity. That is, the model includes the coherent stirring energy implicitly through the
 148 model breakdown parameter \mathbb{I}_M . Figure 3 presents a cartoon of the simplified model.
 149 Note that the evolution of e and T are dependent on the density field creating a coupled
 150 dynamical system for T, e and ρ . As discussed above, the coherent energy T does not
 151 directly mix the density field (ρ), but acts as a propagating source for e .

This model can be written as a system of three couple differential equations:

$$\partial_t T = \mathbb{A} - \mathbb{I}_M + \mathbb{S}, \quad \partial_t e = \mathbb{D}_e - \epsilon - g\mathbb{B} + \mathbb{I}_M, \quad \partial_t \rho = -\partial_z \mathbb{B} + \mathbb{D}_\rho. \quad (3.1)$$

152 The non-turbulent vortex ring energy density (T) is produced (\mathbb{S}), is advected (\mathbb{A}), and
 153 will, in the presence of the stratification, feed the stirring energy, e , at a rate \mathbb{I}_M . The
 154 stirring energy then diffuses (\mathbb{D}_e), dissipates (ϵ), and produces BPE via an irreversible
 155 buoyancy flux (\mathbb{B}) that raises the centre of mass of the density field ρ . That is, \mathbb{B} is
 156 positive semi-definite. Finally, the density field also diffuses (\mathbb{D}_ρ). Each of the operators,
 157 described above, will vary with the vertical coordinate z and time t .

Balmforth *et al.* (1998) constructed a turbulence model that coupled the horizontally-
 averaged turbulent kinetic energy and the density (buoyancy) field. That model depends
 critically on a mixing length scale l , over which the turbulent eddies can mix the sur-
 rounding fluid. We follow an approach similar to Balmforth *et al.* (1998) to model e and
 ρ . In this formulation, we write:

$$\mathbb{D}_e = \partial_z [(\nu_e + \nu) \partial_z e], \quad \epsilon = \beta \frac{e^{\frac{3}{2}}}{l}, \quad \mathbb{B} = -\alpha \nu_e \partial_z \rho, \quad (3.2)$$

$$\mathbb{D}_\rho = \kappa \partial_z^2 \rho. \quad (3.3)$$

Here, we have augmented the previous model with an explicit kinematic viscosity (ν)

		a (10^{-3} m)	U (10^{-3} m/s)	$\Delta\rho$ (10^{-5} kg/m ³)	A (m ²)	Re	Ri	Sc	Notes
Phys. Exp.	E1	45.2 \pm 1.6	37.1 \pm 1.0	1.5 - 3.9	0.4 \times 0.2	1700	4.8-12.3	700	
	E2	48.3 \pm 1.5	39.0 \pm 1.5	2.1 - 4.1	0.4 \times 0.2	1900	3.1-6.5	700	
	E3	50.6 \pm 0.5	54.2 \pm 1.8	1.1 - 3.8	0.4 \times 0.2	2700	3.1-11.7	700	
	E4	49.9 \pm 0.6	49.8 \pm 3.3	1.8 - 7.4	0.45 \times 0.45	2500	3.5-14.6	700	
Num. Exp.	N1	(70)	25.0	0.5 - 2	0.1 \times 0.1	1750	5.8-22.8	3	Resolution 128x128x512 τ (s) 30
	N2	(70)	37.5	0.5 - 2	0.1 \times 0.1	2625	2.5-10.2	3	128x128x512 30
	N3	(70)	50.0	0.5 - 4	0.1 \times 0.1	3500	1.4-11.2	3	192x192x768 40
	N4	33.1	70.8	1-6	0.1 \times 0.1	2343	1.3-3.9	3	128x128x512 40
Model Exp.	M1	40	40	1 - 8	0.4 \times 0.2	1600	2.5-19.6	1000	
	M2	20	20	1 - 8	0.4 \times 0.2	400	4.9-39.2	1000	
	M3	40	40	1 - 8	0.4 \times 0.2	1600	2.5-19.6	3	
	M4	40	40	1 - 8	0.4 \times 0.2	1600	2.5-19.6	1000	Linear Strat.

Vortex-Ring Model

Table 1: Table of the relevant characteristic parameters of the different vortex-ring cases. Data from the physical experiments was taken from Olsthoorn & Dalziel (2015). Note that the diameter of the Hill's vortex ring (highlighted (\cdot)) is defined as $2R$.

	L (m)	z_0 (m)	σ_ρ (m)	H_0 (m)	τ_R (s)
Num. Exp.	0.5	0.375	0.02	0.15	30-40
Model Exp.	0.35	0.3	0.02	0.15	30

Table 2: Table of the dimensional domain parameters for the model and numerical simulation.

and molecular diffusivity (κ). Both e and ρ are primarily driven by eddy diffusion, defined in terms of a turbulent viscosity that, on dimensional grounds, is given as $\nu_e = l\sqrt{e}$. The turbulent dissipation (ϵ) and buoyancy flux (\mathbb{B}) are similarly constructed. The parameters α and β are model constants and will be discussed below. Finally, the non-dimensional turbulent length scale (l) will depend on the local density gradient. For a nearly uniform density field, this length scale will be set by the vortex ring diameter ($l = a$). However, where there is a strong density gradient, the vertical length scales are constrained. The experimental work of Park *et al.* (1994) suggested that, in a strongly stratified environment, the turbulent length scale will be proportional to $\frac{e}{\sqrt{g|\partial_z\rho|}}$. As such, Balmforth *et al.* (1998) proposed a simple model for the length scale that preserves these limits,

$$l = \frac{a\sqrt{e}}{\sqrt{e - \gamma g \partial_z \rho}}, \quad (3.4)$$

158 with free parameter γ .

To model the vortex-ring system, we need to augment this model with the input of energy from the vortex ring, T . We define the advection \mathbb{A} and breakdown \mathbb{I}_M terms as:

$$\mathbb{A} = U \partial_z T, \quad \mathbb{I}_M = \lambda g \left(\frac{\rho - \rho_1}{\rho_0} \right) \sqrt{T}. \quad (3.5)$$

159 The density $\rho_1 = \rho(z = z_0)$ is the density at the vortex ring initialization height z_0 . The
 160 advection term (\mathbb{A}) prescribes that T is transported vertically downward at the constant
 161 propagation speed U . Based upon the work of Olsthoorn & Dalziel (2017), we know
 162 that the stratified vortex-ring system is unstable, with a growth rate proportional to the
 163 bulk Richardson number of the flow. The parameterization of \mathbb{I}_M , which is constructed
 164 on dimensional grounds, captures this dependence (see below) with constant λ , a free
 165 parameter that we will set to unity.

Finally, we must prescribe the generation rate \mathbb{S} of the vortex rings. In this model, T is forced periodically and instantaneously. That is, after each time interval $\Delta t = \tau_R$, a vortex ring is instantaneously introduced into the system. Mathematically, this is written as

$$\mathbb{S} = \sum_{n=0}^N \frac{\text{KE}_{\text{Ring}}}{Aa} f(z - z_0) \delta(t - n\tau_R). \quad (3.6)$$

166 Here, A is the plan area of the stratified tank and δ is a Dirac delta function. The system
 167 is periodically forced for a specified number of iterations N . The index n is the vortex-
 168 ring generation number, which identifies the number of vortex rings that have been input
 169 into the system. The functional form of $f(z)$ is defined below.

We non-dimensionalize the physical parameters as

$$z' = \frac{z}{a}, \quad t' = \frac{U}{a}t, \quad (3.7)$$

$$T' = \frac{T}{U^2}, \quad e' = \frac{e}{U^2}, \quad \rho' = \frac{\rho - \rho_0}{\rho_2 - \rho_0}, \quad (3.8)$$

$$\Delta\rho' = \frac{\rho_2 - \rho_0}{\rho_0}, \quad \tau = \frac{U\tau_R}{a}, \quad K' = \frac{\text{KE}_{\text{Ring}}}{\rho_0 U^2 A a}, \quad (3.9)$$

where the reference density ρ_0 is selected to be the initial minimum density of the system. Similarly, $\Delta\rho'$ is defined as the difference between the initial maximum and minimum density of the system, from which we specify an initial Richardson number $\text{Ri}_0 = g \frac{\rho_2 - \rho_0}{\rho_0} \frac{a}{U^2}$. Finally, K' is the non-dimensionalized kinetic energy of the vortex ring. The model then reduces to the following, dropping the primes for convenience:

$$\partial_t T = \partial_z T - \lambda \text{Ri}_0 (\rho - \rho_1) \sqrt{T} + \sum_{n=0}^N K f(z - z_0) \delta(t - n\tau), \quad (3.10)$$

$$\partial_t e = \partial_z \left[\left(\nu_e + \frac{1}{\text{Re}} \right) \partial_z e \right] - \beta \frac{e^{\frac{3}{2}}}{l} + \alpha \text{Ri}_0 \nu_e \partial_z \rho + \lambda \text{Ri}_0 (\rho - \rho_1) \sqrt{T}, \quad (3.11)$$

$$\partial_t \rho = \partial_z \left[\left(\alpha \nu_e + \frac{1}{\text{Re Sc}} \right) \partial_z \rho \right]. \quad (3.12)$$

The functional form of f is then given:

$$f(z) = \frac{1}{\sqrt{2\pi\sigma^2}} \exp \left[-\frac{z^2}{2\sigma^2} \right], \quad (3.13)$$

170 Here, $\sigma = \frac{1}{4}$ such that the width of the forcing equals the vortex ring size.

171 This model has four free parameters. The work of Tominaga & Stathopoulos (2007)
 172 has shown that the turbulent Schmidt (Prandtl) number α has a typical value of 0.2-
 173 1.3, depending on the flow structure. For the purposes of this model, we set $\alpha = 1$. As
 174 reported in Vassilicos (2015) for decaying turbulence, the dissipation parameter β , where
 175 it is constant, has a value near one, and thus we set $\beta = 1$. With reference to Park *et al.*
 176 (1994), the parameter γ is order one, and thus we set this parameter to one. Based upon
 177 the work of Olsthoorn & Dalziel (2017), we suggest that the value of λ is also $O(1)$. The
 178 vortex breakdown parameter λ is therefore also set to one. Thus, in this paper we restrict
 179 ourselves to the case where the free parameters are all set to unity. We return to this
 180 later.

181 The model was implemented on a uniform grid, using pseudospectral spatial derivatives
 182 and a first-order semi-implicit time stepping scheme. The computational domain was
 183 defined with 1024 grid points. Varying the number of grid points demonstrated that this
 184 resolution was sufficient for the parameter sets presented here. The code was shown to
 185 preserve mass to near machine precision. Adaptive time stepping was used to control the
 186 total energy conservation, which had a relative energy loss typically within $O(10^{-4})$. A
 187 spectral filter was also used to limit the aliasing of the Fourier modes.

We ran a set of model experiments (runs) in a manner similar to that described
 for the physical experiments in §2. Four parameter cases were performed, which pre-
 scribe the functional form of the stratification and the vortex-ring parameters. We label
 these model cases M1-M4. For each of these cases, four different stratification strengths
 ($\Delta\rho = \{0.01, 0.02, 0.04, 0.08\}$) were set, resulting in a total of 16 runs. As described in
 §2, each model run will comprise of sequentially generated vortex rings enumerated as

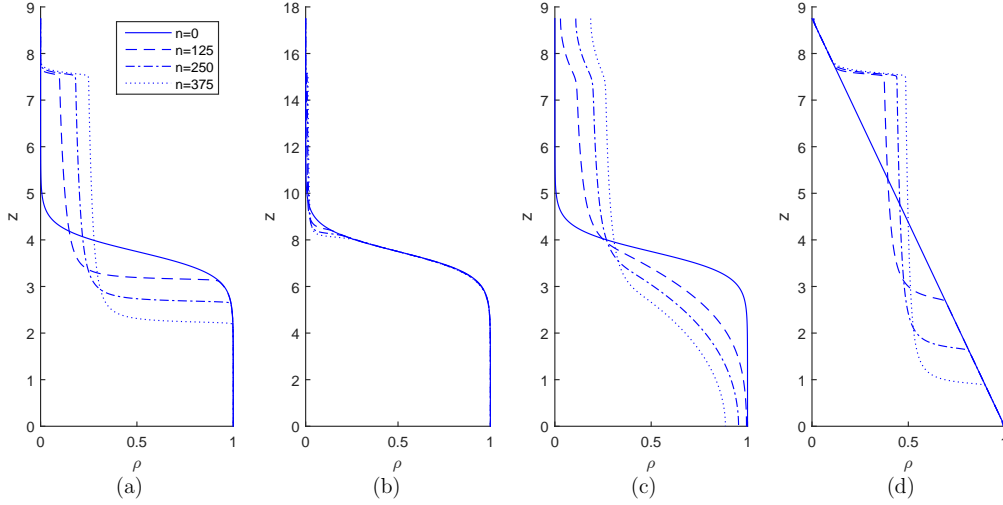


Figure 4: Plot of the evolution of the density profiles for one run ($\Delta\rho = 0.01$) from each of the model cases. Here, model experiments (a) M1, (b) M2: High Ri, (c) M3: Low Sc, and (d) M4: Linear Stratification are all presented. Density profiles are plotted just prior to the generation of vortex ring $n = \{0, 125, 250, 375\}$.

$n = \{0, 1, 2, \dots, N\}$, for a total of $N = 500$ generated vortex rings in each of the 16 runs, as prescribed by equation (3.13). The parameters associated with each of these runs are presented in table 1. In the first three model cases (M1-M3), similar to the experiments of Olsthoorn & Dalziel (2015), a continuous two-layer density profile was specified using a tanh function, with an initial interface height of H_0 and an interface thickness of σ_ρ . These density profiles are prescribed as

$$\rho_{M1-M3}(z, t = 0) = \frac{1}{2} \left(1 - \tanh \left[\frac{z - H_0}{\sigma_\rho} \right] \right). \quad (3.14)$$

The dimensionalized initial conditions are given in table 2 and were selected to approximate the physical experiments performed with salt-water in Olsthoorn & Dalziel (2015). The fourth case (M4) was initialized with a linear stratification, given

$$\rho_{M4}(z, t = 0) = (z - L). \quad (3.15)$$

188 Here, L is the height of the domain.

189 Figure 4 shows the evolution of the density profiles for one run ($\Delta\rho = 0.01$) from
 190 each of the four model cases. Density profiles were plotted just prior to the generation
 191 of vortex ring $n = \{0, 125, 250, 375\}$. The results show excellent qualitative agreement
 192 with the physical experiments. We observe that, as in Olsthoorn & Dalziel (2015), the
 193 evolution of the density profiles is defined by three generic characteristics. First, the
 194 vortex rings sharpen the density interface. Second, the vortex rings generate a middle
 195 fluid layer that is near homogeneously mixed. Third, the growth of the middle fluid layer
 196 is limited by the vortex ring injection height.

197 Comparison of figure 4(a)(Model Exp. M1) and figure 4(b)(M2) demonstrates how
 198 the density field evolution changes for different vortex ring parameters (M1 : Re =
 199 1600, Ri = 2.5 versus M2 : Re = 400, Ri = 4.9). The same characteristic evolution of the

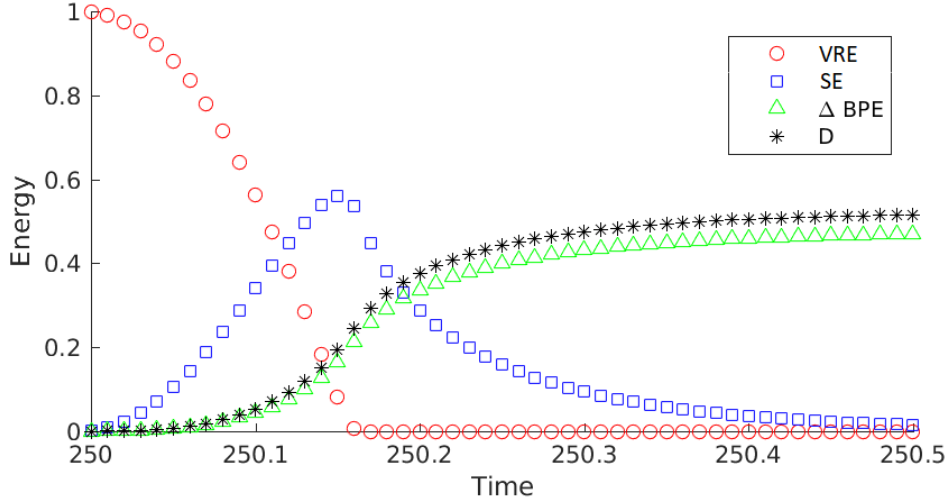


Figure 5: Plot of the partition of energy between the integrated vortex-ring energy (VRE) and stirring energy (SE) for vortex ring $n = 250$. The change in potential energy (ΔBPE) and the integrated dissipation (D) are also plotted. Time has been normalized by the inter vortex-ring spacing τ . Data has been plotted for M1 with $\Delta\rho = 0.01$.

200 density profiles is observed for M2, though only a small amount of scouring of the density
 201 interface has occurred due to the decrease in kinetic energy input. Figure 4(c)(M3) varies
 202 the molecular diffusivity (κ) of the stratification ($\text{Sc} = 3$ versus $\text{Sc} = 1000$). Again, the
 203 same features of the density profiles are observable, except that the vortex rings are
 204 no longer able to effectively sharpen the lower interface as it diffuses. Due to the finite
 205 domain size, significant diffusion of the density interface can limit the run time of the
 206 model. This will be important when discussing the numerical simulations below. Finally,
 207 figure 4(d)(M4) encapsulates the effect of a different initial background stratification
 208 (linear profile), demonstrating the same characteristic evolution, although we have no
 209 matching physical experiments against which to compare these runs.

210 Figure 5 shows the partition of energy for the model experiments for a single mixing
 211 event ($n = 250$) of M1 ($\Delta\rho = 0.01$). This shows the integrated vortex-ring energy (VRE
 212 $= \int_0^L T dz'$) and integrated stirring energy ($\text{SE} = \int_0^L e dz'$), along with the change
 213 in background potential energy (ΔBPE) of the system (correcting for the background
 214 diffusion \mathbb{D}_ρ). The integrated dissipation ($D = \int_{t_n}^t \int_0^L \epsilon dz' dt'$) has also been plotted. We
 215 observe that the mixing is temporally confined near the peak in e , as emphasized in §2.
 216 However, data on the time-dependent dissipation and mixing rates are not available for
 217 the physical experiments and thus comparison is limited to that of the density profiles
 218 $\rho(z, t)$.

219 4. Simulation of the Vortex-Ring-Induced Mixing Experiments

We validate the 1D model results using a 3D pseudospectral numerical solver (SPINS;
 see Subich *et al.* (2013)) to solve the incompressible Navier-Stokes equations under the

Boussinesq approximation. These equations can be written as

$$(\partial_t + \mathbf{u} \cdot \nabla) \mathbf{u} = -\nabla p - \text{Ri} \rho g \hat{\mathbf{z}} + \frac{1}{\text{Re}} \nabla^2 \mathbf{u}, \quad (4.1)$$

$$(\partial_t + \mathbf{u} \cdot \nabla) \rho = \frac{1}{\text{Re Sc}} \nabla^2 \rho, \quad (4.2)$$

$$\nabla \cdot \mathbf{u} = 0. \quad (4.3)$$

220 Here, \mathbf{u} and p are the velocity and pressure fields, respectively. Boldface variables denote
221 vector quantities.

222 Experimental visualizations of the interaction of a vortex ring with a stratified inter-
223 face (see Olsthoorn & Dalziel (2017)) demonstrate that, where the vortex ring propagates
224 parallel to the direction of gravity, the flow field remains predominantly axisymmetric
225 about the vortex ring axis throughout the majority of the interaction, despite the forma-
226 tion of a three-dimensional instability. In order to facilitate the numerical computations,
227 we take partial advantage of this symmetry by simulating a quarter ring in a triply peri-
228 odic, free-slip (cosine transform) domain. The parameters associated with the numerical
229 simulations can be found in table 1. Grid resolution studies determined that the resolu-
230 tion (see table 1) was sufficient to estimate the mixing efficiency, although we note that
231 we do not resolve down to the Batchelor scale of the flow. As with the model results,
232 a high molecular diffusivity results in a thick density interface, which will eventually
233 violate the continuous two-layer setup considered here, and will limit the run-time of
234 each experiment. Thus, we desire the lowest diffusivity that is computationally viable. In
235 these simulations, we select $\text{Sc} = 3$. Four sets of numerical simulations were performed.
236 The initial density stratification for each case was defined via a tanh profile similar to
237 (3.14). See table 2 for the initial conditions.

Three sets of simulations (Num. Exp. N1-N3) were initialized with a Hill's spherical
vortex as it is a classical vortex ring solution. The Hill's vortex can be written as

$$u_r = \begin{cases} \frac{3}{2} U \frac{zr}{R^2} & r \leq R \\ \frac{3}{2} U \frac{zr}{R^2} \left(\frac{R^2}{z^2+r^2} \right)^{\frac{5}{2}} & r > R \end{cases}, \quad u_z = \begin{cases} \frac{3}{2} U \left(\frac{5}{3} - \frac{2r^2+z^2}{R^2} \right) & r \leq R \\ U \left[\left(\frac{R^2}{r^2+z^2} \right)^{\frac{5}{2}} \left(\frac{2z^2-r^2}{2R^2} \right) - 1 \right] & r > R \end{cases}.$$

238 In this paper, R is the radius of the Hill's vortex, and $U < 0$ is its propagation speed. We
239 note that there is a mismatch between the definition of the Hill's vortex diameter ($2R$)
240 and the experimentally measured vortex-ring diameter that was defined as the distance
241 between vorticity centroids (see Olsthoorn & Dalziel (2015)). A random initial velocity
242 perturbation of $O(10^{-4})$, relative to the vortex-ring propagation speed, was added to the
243 numerical simulations in order to trigger any instabilities in the interaction between the
244 vortex ring and the stratification.

245 For the fourth set of simulations (N4), a different initial condition was used to assess
246 the dependence of the results on the ring aspect ratio (core size/ring diameter). Similar
247 to Archer *et al.* (2009), a vorticity distribution was initialized into the numerical solver
248 (we used an azimuthally rotated shielded dipole) that, when time evolved, produced a
249 coherent vortex ring. This resultant non-spherical vortex ring was then used as the initial
250 condition for the numerical mixing simulations. Fitting the vortex core to a Gaussian
251 distribution, we estimate the aspect ratio of this vortex ring to be 0.17. In the physical
252 experiments, the vortex rings had an aspect ratio of ≈ 0.1 .

253 As with the experimental setup described in §2, and the model setup described in §3,
254 the simulations were run by generating vortex rings that interact with the stratification.
255 The flow was then evolved until the velocity field dissipated sufficiently. After a delay

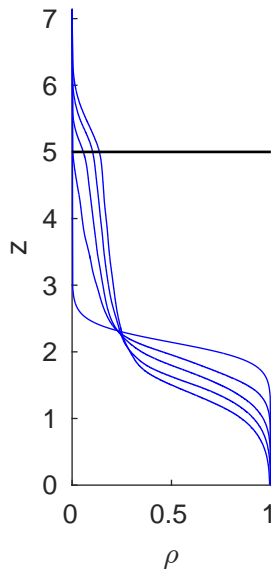


Figure 6: Plot of the sorted density profile every twenty vortex ring generations of one numerical simulation (N3: $Re = 3500$, $Ri = 2.75$). A solid line is drawn at $z = z_0$.

256 (τ), the velocity field for a new vortex ring was superimposed (by addition) onto the
 257 residual velocity field. This cycle was repeated until the desired number of iterations
 258 was achieved. We set the end time to be 100 vortex rings. Thirteen different parameter
 259 cases (requiring 1300 simulations) were performed for various Reynolds and Richardson
 260 numbers, the details of which can be found in table 1. As with the experimental results of
 261 Olsthoorn & Dalziel (2015) and the model results above, there is an initial setup period,
 262 within which the functional form of the stratification varies. After this setup period, the
 263 stratification tends to a self-similar form and the mixing rate is nearly constant, and it
 264 is this value that is reported.

265 Figure 6 shows the sorted density profile every 20 vortex ring generations for one
 266 numerical simulation (N3: $Re = 3500$, $Ri = 2.75$). Here, we again observe the same char-
 267 acteristic features of the background density field evolution. Note the similarity between
 268 figure 4(c) and figure 6. As before, the diffusion of the background stratification is signif-
 269 icant and must be accounted for when considering the mixing rate of each vortex ring.
 270

271 Additionally, figure 7(a) shows the evolution of the distribution of energy into its var-
 272 ious compartments for the first vortex ring of one numerical simulation (N3: $Re = 3500$,
 273 $Ri = 2.75$). This figure is reminiscent of figure 5 from the model results. In particular,
 274 the time dependence of the mixing (M) and the total dissipation (D) provided in figure
 275 7(a) are similar to those found previously in figure 5, though their relative values are
 276 different. Unlike the model, the numerical simulations explicitly support the generation
 277 of APE. Associated with this APE is the generation of internal waves that manifest
 278 as oscillations between the APE and the kinetic energy (KE). Figure 7(b) shows the
 279 relative energy distribution prior to the generation of a new vortex ring, for all vortex
 280 ring generations. This plot quantifies the incremental change to the mixing rate of each
 281 subsequent vortex ring. Both panels (a)-(b) have been normalized by the initial vortex-
 282 ring energy (E) and the interval τ between vortex rings for comparison with the model

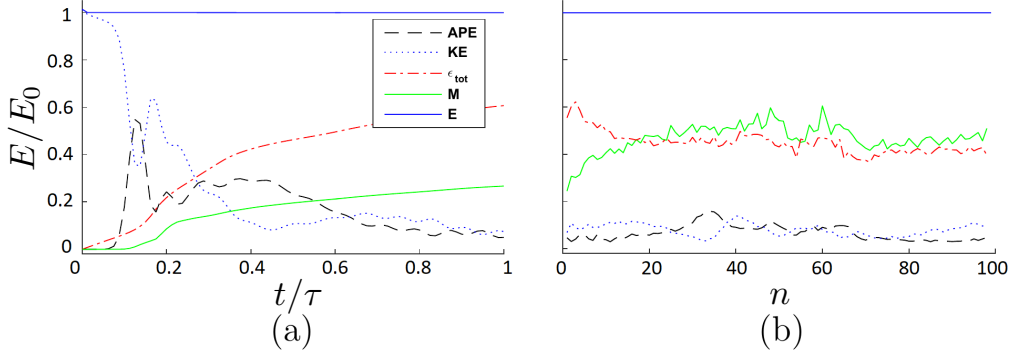


Figure 7: (a) Plot of the energy partition for the first vortex ring interaction of Num. Exp. N3 (N3: $Re = 3500$, $Ri = 2.75$). Note that the KE is initially slightly above 1 as a result of the initial perturbation. (b) Plot of the energy partition at the end of each subsequent n vortex ring interactions.

283 results. Typical net relative energy loss at time $t = \tau$ is 5×10^{-3} . Due to the late-time
 284 exponential decay of the internal waves generated, there will always be some residual
 285 stirring energy ($RE = KE + APE$ at $t = \tau$) in the system prior to subsequent vortex ring
 286 generations. As there is a practical limitation on the length of each numerical simulation,
 287 we terminated the simulations when $\frac{RE}{KE_{ring}} = O(10\%)$. The physical experiments also
 288 have RE, though it is much less than that of the numerical simulations, as we can wait
 289 longer between vortex ring generations at almost no cost. As this residual energy remains
 290 nearly constant with subsequent vortex ring generations, the RE will have a small, near
 291 constant, contribution to the increase in BPE of the system, when compared to the mean
 292 mixing rate of each vortex ring. As mentioned above, these simulations demonstrate an
 293 initialization period, after which the change in potential energy of the system is near
 294 constant.

295 5. Discussion and Conclusion

For each experiment, we compute the ratio of the change in background potential energy (ΔBPE) between successive vortex rings ($\Delta t = \tau$) versus the energy of the input vortex ring (KE_{ring}). We define this ratio as the mixing efficiency (η), indicating the amount of background potential energy change for a given energy input. This definition of the mixing efficiency is unambiguous where $RE = 0$. Where $RE \neq 0$, provided that the RE is constant between vortex ring generations, the associated mixing will also be constant and the interpretation of the mixing efficiency remains well defined over the interval between vortex rings. The mixing efficiency is then computed as

$$\eta = \frac{\Delta BPE - \Delta PE_{\kappa}}{KE_{ring}}, \quad \text{where} \quad \Delta BPE = gA\rho_0\Delta\rho a^2 \int [\rho_s^{(n+1)} - \rho_s^{(n)}] z dz. \quad (5.1)$$

296 Here, $\rho_s^{(n)}$ is the sorted density profile after n vortex rings have been produced. The
 297 change in BPE is corrected for the diffusive increase in potential energy ($\Delta PE_{\kappa} =$
 298 $gA\kappa\tau(\rho(0) - \rho(L))$) as we are interested only in the contribution due to the vortex ring.

299 Comparing the model, numerical simulations and physical experiments, figure 8 shows
 300 the mixing efficiency determined for all cases identified in table 1. In this plot, the mixing
 301 efficiency is near constant with Ri. Error bars are computed as the root mean squared
 302 error from the associated mean mixing efficiency value, once the system has completed its
 303 initial setup period. We observe that the mixing efficiency of the numerical simulations
 304 ($\eta_N \approx 0.45$) is slightly higher than the physical, salt-water experiments ($\eta_0 \approx 0.42$),
 305 as would be expected from the lower Sc. (The computational resources necessary to
 306 use the experimental value of Sc were not available.) The mixing efficiencies found in
 307 the model are consistently higher still ($\eta_M \approx 0.49$) than the numerical simulations or
 308 physical experiments, though it is still within the experimental uncertainty of the physical
 309 experiments.

310 As we have noted previously, the model is dependent on four free parameters ($\alpha, \beta, \gamma, \lambda$).
 311 Figure 9 presents the linear parameter analysis for the four free model parameters. In
 312 each of the four plots, one of the four parameters was varied while the other three were
 313 held constant. In each case the mixing efficiency was computed for one run of case M1
 314 ($\Delta\rho = 0.01$) at $n = 100$. We note that an increase in the dissipation parameter β by
 315 $\approx 15\%$ (see figure 9(b)) would account for the difference between the experimental value
 316 of the mixing efficiency and the model runs. It is worth noting that that the parameters
 317 associated with the dissipation rate are where most of the sensitivity of the model resides.
 318 A more precise parameter selection is left for future work.

319 As the Richardson number decreases below $O(1)$, the mixing efficiency dependence
 320 on Ri becomes more ambiguous. Indeed, recent work by Shrinivas & Hunt (2015) has
 321 indicated that the vertical confinement of turbulent mixing may change the mixing ef-
 322 ficiency dependence on Ri. This confinement will be especially pronounced at low Ri
 323 due to the deep penetration of the vortex rings into the lower layer. The confinement is
 324 entirely omitted in the model due to its 1D construction. As the effect of confinement
 325 will influence the three-dimensional structure of the flow, one might initially model it by
 326 modifying the propagation speed (U) of the vortex rings near the boundaries. We do not
 327 attempt this here.

328 Finally, we want to highlight that the mixing efficiency is defined here as an aggregate,
 329 time-independent quantity. That is, the net fluid mixing that results from a given energy
 330 input. This definition suggests that vortex rings are effective mixers as they transport
 331 energy directly to the density interface (with minimal dissipation), produce vorticity
 332 directly at the location of the peak in the density gradient (which Lawrie & Dalziel
 333 (2011) argued would result in a high mixing efficiency), and, through a flow instability
 334 (see Olsthoorn & Dalziel (2017)), generate turbulence. This series of events enables each
 335 vortex ring to create a near optimal mixing state such that nearly all the vortex ring
 336 energy is deposited directly at the location of peak mixing. That is, the kinetic energy
 337 of the vortex ring produces stirring energy at the location of peak density gradient.
 338 In addition, turbulent stirring energy is generated at a rate proportional to the bulk
 339 Richardson number of the system, which is essential for the system to establish a self-
 340 similar density profile. The model, which is a simplification of the vortex ring system,
 341 emphasizes this picture by only generating stirring energy (at a rate proportional to
 342 the bulk Richardson number) where the density field is not constant; where mixing can
 343 occur. This is in contrast to grid generated turbulence, which dissipates significantly
 344 before reaching the density interface.

345 This paper presents a model for isolated vortex-ring-induced stratified mixing exper-
 346 iments. This work has been shown to provide qualitative and quantitative agreement
 347 with both physical experiments and numerical simulations. At moderate Ri, the mixing
 348 efficiency of the vortex rings has been shown, in all three methodologies, to be near con-

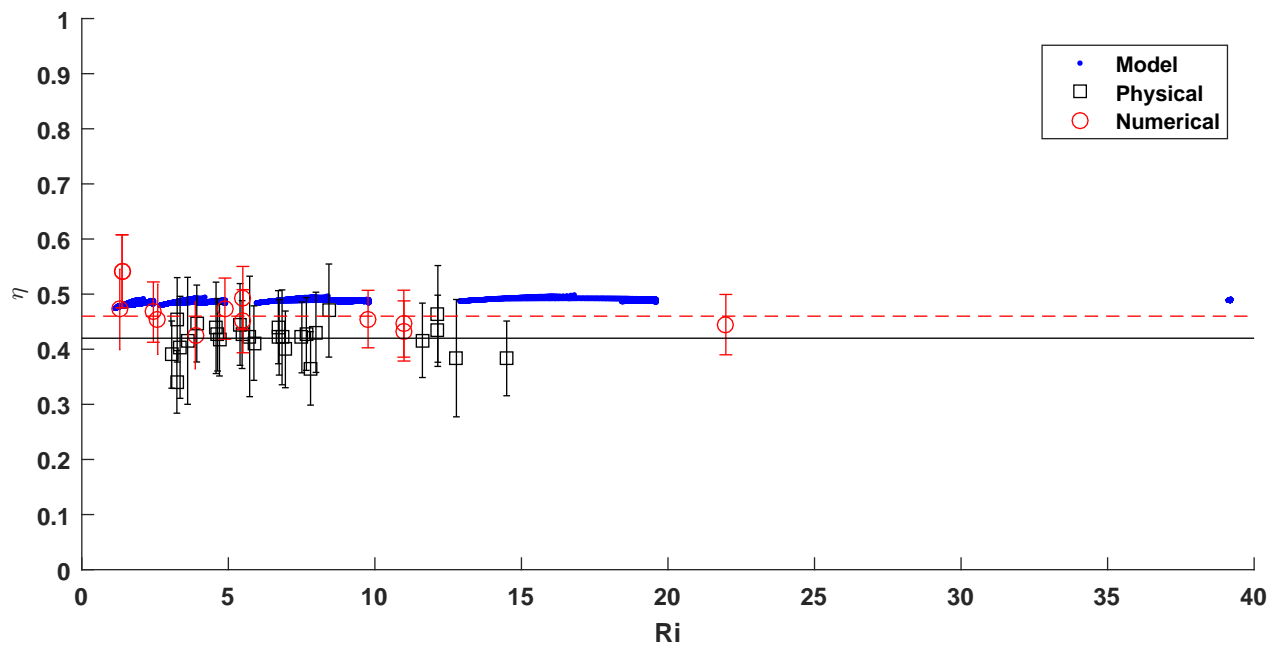


Figure 8: Mixing efficiency as a function of Richardson number for the model, numerical simulations, and physical experiments found in table 1. The black solid line corresponds to the mean mixing efficiency of the physical experiments ($\eta_0 = 0.42$). The dashed red line is the estimated mixing efficiency of the numerical simulations ($\eta_N = 0.45$).

stant after an initialization period with very similar asymptotic values. This constant
 mixing efficiency regime of the vortex-ring experiments has been previously reported in
 Olsthoorn & Dalziel (2015), although the numerical work found in this paper demon-
 strates this regime at a much lower Schmidt number ($Sc = 3$ versus $Sc = 700$). The 1D
 model constructed in the paper encapsulates the essential features of the energy pathways
 for the vortex-ring-induced mixing experiments. In particular, this work highlights the
 important contribution of the vortex-ring breakdown being proportional to the Richard-
 son number ($\mathbb{I}_M \propto Ri_0$). As demonstrated in Olsthoorn & Dalziel (2017), the dominant
 vortex-ring instability in the strongly stratified system ($Ri > O(1)$) has a growth rate
 proportional to the bulk Richardson number of the flow. This model demonstrates that
 the identified vortex-ring instability plays a key role in establishing the constant mixing
 efficiency regime.

We study vortex-ring-induced mixing in analogy to large-scale turbulent-eddy mixing
 events. However, it should be clear that stratified turbulence is characterized by its
 large range of length scales and complex flow structures. As such, a natural extension
 of the present model would investigate a convolution of the individual mixing events
 discussed here. Future work will investigate the application of this model to a mixing
 box experiment, similar to the one described in Turner (1968).

6. Acknowledgments

Support for this work was provided by the Natural Sciences and Engineering Research
 Council of Canada (NSERC) and through the Engineering and Physical Sciences Re-
 search Council (EPSRC) grant number EP/L504920/1. Additional support has been
 provided by the EPSRC Mathematical Underpinnings of Stratified Turbulence grant
 EP/K034529/1. Portions of the data associated with this paper can be found in the
 repository XXXXXXXXXXXXXXXX.

REFERENCES

- ARCHER, P. J., THOMAS, T. G. & COLEMAN, G. N. 2009 The instability of a vortex ring
 impinging on a free surface. *Journal of Fluid Mechanics* **642**, 7994.
- BALMFORTH, N. J., LLEWELLYN SMITH, STEFAN G. & YOUNG, W. R. 1998 Dynamics of
 interfaces and layers in a stratified turbulent fluid. *Journal of Fluid Mechanics* **355**, 329–
 358.
- FERNANDO, HARINDRA JS 1991 Turbulent mixing in stratified fluids. *Annual review of fluid
 mechanics* **23** (1), 455–493.
- IVEY, G.N., WINTERS, K.B. & KOSEFF, J.R. 2008 Density stratification, turbulence, but how
 much mixing? *Annual Review of Fluid Mechanics* **40** (1), 169–184.
- LAWRIE, ANDREW G. W. & DALZIEL, STUART B. 2011 Turbulent diffusion in tall tubes. i.
 models for rayleigh-taylor instability. *Physics of Fluids* **23** (8), 085109.
- LINDEN, P. F. 1973 The interaction of a vortex ring with a sharp density interface: a model for
 turbulent entrainment. *Journal of Fluid Mechanics* **60**, 467–480.
- LINDEN, P. F. 1979 Mixing in stratified fluids. *Geophysical and Astrophysical Fluid Dynamics*
13 (1), 3–23.
- NORBURY, J. 1973 A family of steady vortex rings. *Journal of Fluid Mechanics* **57**, 417–431.
- OLSTHOORN, JASON & DALZIEL, STUART B. 2015 Vortex-ring-induced stratified mixing. *Journal
 of Fluid Mechanics* **781**, 113–126.
- OLSTHOORN, JASON & DALZIEL, STUART B. 2017 Three-dimensional visualization of the inter-
 action of a vortex ring with a stratified interface. *Journal of Fluid Mechanics* **820**, 549–579.
- PARK, YOUNG-GYU, WHITEHEAD, J. A. & GNANADESKIAN, ANAND 1994 Turbulent mixing in
 stratified fluids: layer formation and energetics. *Journal of Fluid Mechanics* **279**, 279–311.

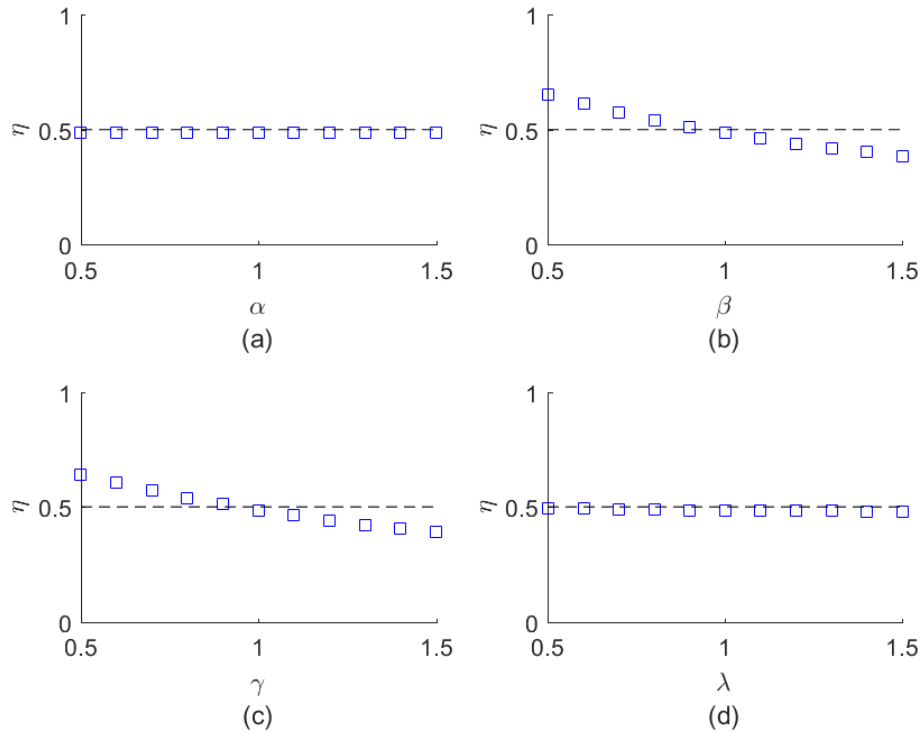


Figure 9: The dependence of the mixing efficiency on the model parameters (a) α , (b) β , (c) γ , and (d) λ . A dashed line has been plotted at $\eta = 0.5$. Mixing efficiency values were generated from case M1 ($\Delta\rho = 0.01$) at $n = 100$.

- 396 SHRINIVAS, A. B. & HUNT, G. R. 2015 Confined turbulent entrainment across density interfaces.
 397 *Journal of Fluid Mechanics* **779**, 116–143.
- 398 SUBICH, C. J., LAMB, K. G. & STASTNA, M. 2013 Simulation of the navierstokes equations in
 399 three dimensions with a spectral collocation method. *International Journal for Numerical*
 400 *Methods in Fluids* **73** (2), 103–129.
- 401 TOMINAGA, YOSHIHIDE & STATHOPOULOS, TED 2007 Turbulent schmidt numbers for {CFD}
 402 analysis with various types of flowfield. *Atmospheric Environment* **41** (37), 8091 – 8099.
- 403 TURNER, J. S. 1968 The influence of molecular diffusivity on turbulent entrainment across a
 404 density interface. *Journal of Fluid Mechanics* **33**, 639–656.
- 405 VASSILICOS, J. CHRISTOS 2015 Dissipation in turbulent flows. *Annual Review of Fluid Mechanics*
 406 **47** (1), 95–114.
- 407 WINTERS, K. B., LOMBARD, P. N., RILEY, J. J. & D’ASARO, E. A. 1995 Available potential
 408 energy and mixing in density-stratified fluids. *Journal of Fluid Mechanics* **289**, 115–128.